

What can the kinetics of amyloid fibril formation tell about off-pathway aggregation?

Rosa Crespo¹, Eva Villar-Alvarez², Pablo Taboada², Fernando A. Rocha¹, Ana M. Damas³ and Pedro M. Martins^{1,3}

¹From LEPABE, Laboratório de Engenharia de Processos, Ambiente, Biotecnologia e Energia, Departamento de Engenharia Química, Faculdade de Engenharia da Universidade do Porto. Rua Dr. Roberto Frias, 4200-465 Porto, Portugal

²Departamento de Física de la Materia Condensada, Facultad de Física, Universidad de Santiago de Compostela, Spain

³ICBAS – Instituto de Ciências Biomédicas Abel Salazar, Universidade do Porto, Porto, Portugal

Running title: *How to screen amyloid off-pathway modulators*

To whom correspondence should be addressed: Pedro M. Martins, ICBAS – Instituto de Ciências Biomédicas Abel Salazar, Universidade do Porto, Rua de Jorge Viterbo Ferreira n.º 228, 4050-313 Porto, Portugal, Tel.: (+351) 220428137; E-Mail: pmmartins@icbas.up.pt

Keywords: Amyloid, protein aggregation, biophysics, mathematical modeling, kinetics, drug screening

ABSTRACT

Some of the most prevalent neurodegenerative diseases are characterized by the accumulation of amyloid fibrils in organs and tissues. While the pathogenic role of these fibrils is not totally established, increasing evidences suggest off-pathway aggregation (OPA) as a source of toxic/detoxicating deposits that still remains to be targeted. The present work is a step ahead towards the development of off-pathway modulators using the same amyloid-specific dyes as those conventionally employed to screen amyloid inhibitors. We identified a series of kinetic signatures revealing the quantitative importance of OPA relatively to amyloid fibrillization; these include non-linear semi-log plots of amyloid progress curves, highly variable endpoint signals and half-life coordinates weakly influenced by concentration. Molecules that attenuate/intensify the magnitude of these signals are considered promising off-pathway inhibitors/promoters. An illustrative example shows that amyloid deposits of lysozyme are only the tip of an iceberg hiding a crowd of insoluble aggregates. Thoroughly validated using advanced microscopy techniques and complementary measurements of Dynamic Light Scattering (DLS), Circular Dichroism (CD) and soluble protein depletion, the new analytical tools are compatible with the high-throughput methods currently employed in drug discovery.

Nucleation and growth mechanisms are ubiquitous in nature, from atmospheric aerosol formation (1) to microtubule polymerization in eukaryotic cells (2) and biomineralization (3). The present work focuses amyloid fibril formation as a particular case of such phase transition phenomena. Amyloid fibrils are filamentous assemblies of proteins in which the polypeptide backbone is arranged in a characteristic cross- β -sheet structure running perpendicular to the long axis of the fibrils. Despite the conflicting evidence about its pathogenic role (4), the accumulation of amyloid deposits in a variety of organs and tissues is associated to the most prevalent neurodegenerative diseases and to amyloidosis (5). Intermediate oligomeric species and off-pathway end-products may, however, be more dangerous for the development of amyloid diseases than mature fibrils themselves (4,6,7,8,9). Conversely, the aggregation pathway might be redirected into insoluble oligomers less toxic than amyloid fibrils (10), given that both types of precipitates kinetically compete for soluble protein (11). As non-fibrillar species are also hard to detect, the molecular mechanisms involved in their formation are particularly difficult to infer (12,13,14). Their existence should, at any rate, be a disturbance to the otherwise predictable sigmoidal to hyperbolic kinetics of phase transition.

By lacking the cross- β -sheet structure, intermediate and off-pathway species cannot be identified using amyloid-specific dyes such as

fluorescent thioflavin-T (ThT). If solely amyloid-like fibrils are produced, the development of the mass-of-aggregates signal will be equivalent to the depletion of protein monomers in solution (15). Both macroscopic indicators should be the result of "direct" phase transition events of primary (concentration-driven) nucleation, secondary (autocatalytic) nucleation and fibril growth (or elongation). Other "indirect" events, including fibril fragmentation and association, do not involve the transition of molecules between phases and, therefore, do not affect the reciprocity between aggregation of fibrils and depletion of protein. Proposed in 2012, the "crystallization-like model" (CLM) describes how the molecular mechanisms of nucleation and growth affect the evolution of amyloid conversion (α) with time (t). The two-parameter CLM equation for unseeded reactions reads (16):

$$\alpha = 1 - \frac{1}{k_b(e^{k_a t} - 1) + 1} \quad (1)$$

where k_a , originally called the growth rate constant, is more broadly defined as the autocatalytic rate constant since it can also include the contribution of secondary nucleation steps proportional to the amount of amyloid fibrils in solution. The parameter k_b gives the relative rates of primary nucleation steps over autocatalytic steps. Once demonstrated the ability of the CLM to describe traditional fibrillization kinetics (16) and discriminate between true and apparent amyloid inhibitors (17), new CLM-based tools are hereby proposed in order to identify off-pathway processes. A preliminary note is, however, required in order to define what are the regular kinetic behaviors expected in the absence of parallel aggregation.

The current understanding of the kinetics and thermodynamics of protein aggregation was comprehensively reviewed by Morris, Watzky and Finke (18), and more recently, by Gilliam and MacPhee (15). The standard sigmoidal growth curve exhibiting an initial lag-phase followed by a period of rapid growth and a final plateau phase is, in general, satisfactorily fitted by the existing theoretical models, which gives rise to different explanations of the same result. There are, however, a number of other common behaviors that remain unexplained, even by the more

sophisticated models (15). Some of these inconsistencies are marked in red in Figure 1, where a graphical account of typical experimental results is also provided. The hyperbolic (concave) profiles exhibiting no inflection point or lag-phase in absence of seeding (Fig. 1a) are frequently reported in literature during the aggregation of e.g., serum albumin (19,20), transthyretin (21,22), β_2 -microglobulin (23), the four repeat domain of Tau (24), apolipoprotein (25) and amyloid- β variants (26,27). This kind of results is explained by the CLM as the result of predominant primary nucleation over the autocatalytic processes, and is also well fitted by the "Ockham's Razor" minimalistic model (18,28). According to Oosawa-type models (29) such as those of Ferrone et al. (30) and Knowles et al. (31), the early stage increase of the mass of fibrils cannot occur any faster than by polynomial t^n or exponential $\exp(kt)$ laws during unseeded reactions (15,32). Therefore, Oosawa-type models fail to explain the concave profiles of the form $1 - \exp(-kt)$ shown in red in Figure 1a (15). The CLM advantageously uses fundamental principles of phase transition to explain the nonlinear trends in Figure 1b. By expressing the driving force for protein aggregation as the thermodynamic supersaturation $\sigma = (C - C_a^*)/C_a^*$ (an approximation to the variation in chemical potential), the steady-state monomer concentration is expected to correspond to the amyloid solubility $C_\infty = C_a^*$. At the same time that the CLM was being proposed, Yoshimura et al. urged the need to recognize amyloidogenicity as a property determined by the monomer concentration relative to solubility (33); since then, a wealth of new evidences unanimously confirm supersaturation as a major driving force for protein aggregation (6,11,34,35,36,37,38). Although this parallel with crystallization had been hinted before (21,39), the common practice in literature models is to assume the monomer concentration alone as the driving force for phase transition (18,28,29,30,31) meaning that, e.g., amyloid fibrils would continue to grow until the solution became completely depleted from soluble protein. In addition, the duration of the lag-phase would be a linear function of C_0 when represented in a log-log

scale; this follows from model equations of variable complexity that, in general, can be simplified to a power law equation with a constant scaling exponent γ (15,40). The same does not apply for the CLM, where the lag-times scale exponentially with supersaturation σ_0 rather than with the initial concentration C_0 . The result is a "broken" curve such as those represented in Figure 1b, in which the scaling factor γ changes its value as C_0 decreases to values closer to C_a^* . Note that although the theoretical range of concentrations includes the solubility value, the formation of fibrils by primary nucleation is only expected to occur for C_0 values above a critical concentration higher than C_a^* . The existence of breaks in lag-time versus concentration plots is widely reported in literature as reviewed by Eden et al. (40). The different profiles simulated in Figure 1b result from the influence of the initial supersaturation σ_0 on the primary nucleation rate constant k_b . Both k_a and k_b influence the time needed to reach 50% completion (t_{50}) as determined by the following equation (16):

$$t_{50} = \frac{1}{k_a} \ln \left(\frac{1}{k_b} + 1 \right) \quad (2)$$

While the parameter k_a is proportional to σ_0 , the parameter k_b is proportional to the critical number of monomers constituting the amyloid nucleus n_c , whose variation with σ_0 is not so well established (16). Determining the k_b vs. σ_0 relationship is particularly difficult owing to the amplified uncertainty associated to k_b estimates when sigmoidal aggregation curves are used (16). Apparently in contradiction with the Classical Nucleation Theory, the value of k_b (and n_c) estimated from hyperbolic aggregation kinetics of transthyretin is proportional to σ_0 (16,21). The inset in Figure 1b shows how different values of k_b/σ_0 influences the scaling exponent γ extracted for high monomer concentrations. Sufficiently low k_b/σ_0 values are chosen in order to assure meaningful durations of the lag-phase. Although other scaling behaviors result from admitting different $k_b(\sigma_0)$ functions, the interval of γ values

lying between -2 and -1 is in good agreement with recent Monte Carlo simulations that extend the classical nucleation-elongation-fragmentation scheme to include a stochastic nucleation step (40). Each of the closed-form solutions of Oosawa-type models predicts a different scaling exponent that remains approximately constant over the concentration range (15,41); explaining the existence of broken curves was shown to require additional fundamental insights besides the simple interplay between the different mechanistic alternatives (40,42). In Ockham's Razor-type models, sigmoidal aggregation curves exhibiting pronounced lag-phases correspond to the limit case of very low primary nucleation rates for which the model equations simplify to a logistic function (16). Here again, the exponential factor γ is approximately constant (close to -1) over the concentration ranges that produce lag-phases. A striking result not covered by any of the scenarios in Figure 1b is the weak dependence of the lag-time on concentration with absolute values of γ well below 1 at high monomer concentrations (15,31,40,43). In the case of lysozyme aggregation under harsh denaturing conditions the process becomes nearly concentration independent ($\gamma \approx 0$) for protein concentrations significantly higher than the solubility (40). The formation of intermediate and off-pathway species is a likely explanation of this and of other deviations from canonical kinetics as illustrated next for HEWL aggregation under conditions of low pH (1.6) and high temperature (60 °C) known to produce other aggregates than amyloid fibrils (44,45,46).

EXPERIMENTAL PROCEDURES

Chemicals: HEWL was obtained from Merk KGaA (Darmstadt, Germany). ThT was obtained from Sigma-Aldrich (St Louis, MO, USA) and used as received. Other chemicals were reagent grade and obtained from Merk KGaA (Darmstadt, Germany).

HEWL preparation: HEWL powder was dissolved in 25 mM HCl pH 1.6 and dialyzed against 25 mM HCl, pH 1.6, using a cut-off 3500 Da membrane (Spectrum, Fisher Scientific). The concentration of the dialyzed protein solution was determined by absorbance measurements at 280 nm using an extinction coefficient of 37752 M⁻¹cm⁻¹. Protein

tocks were stored at 4 °C for no longer than one week.

ThT Fluorescence: ThT fluorescence kinetic measurements were carried out at 60 °C in 96-well plates (Thermo Scientific, microtiter) in a CHAMELEON™V Microplate Reader (Hidex Co., Turku, Finland) at an excitation wavelength of 440 nm and an emission wavelength of 485 nm. ThT stock solution was prepared by dissolving the dried powder in 25 mM HCl, pH 1.6, and filtered through a sterile 0.45 µm pore size PES membrane filter (Jet Biofil). The concentration was determined by absorbance measurements at 411 nm using an extinction coefficient of 22000 M⁻¹cm⁻¹. Samples of 120 µl with a final ThT concentration of 2.8 mM and HEWL concentrations of 0.60, 0.93, 1.25, 1.39 and 1.76 mM were sealed with 100 µl of paraffin oil. Measurements were recorded every 1800 s, after sample homogenization by 300s shaking. Data was background-corrected for the ThT fluorescence of the respective solvent in the absence of protein.

Depletion of soluble HEWL: Independent 1.76 mM HEWL samples were incubated at 60 °C and periodically filtered through a sterile 0.22 µm pore size PES membrane filter (Jet Biofil). After 1 hour at room temperature, filtered samples were diluted 1:50 in 25 mM HCl pH 1.6 and analyzed spectrophotometrically at 280 nm using a 1 cm pathlength quartz cuvette (Hellma GmbH & Co. KG, Müllheim, Germany) and an extinction coefficient of 37752 M⁻¹cm⁻¹.

CD: CD experiments were performed using a Jasco J-815 spectropolarimeter (Tokyo, Japan) equipped with a Peltier-controlled thermostated cell support. Independent 1.76 mM HEWL samples were incubated at 60 °C for periods of 1 to 7 days. Samples, were diluted 1:400 in 25 mM HCl, pH 1.6. CD spectra were measured from 190 to 260 nm in a 0.1 cm pathlength quartz cuvette (Hellma Analytics). The final spectrum of all samples was an average of 16 independent scans recorded with 1 nm bandwidth, 2 s digital integration time and a scanning speed of 50 nm/min.

DLS: DLS measurements were performed at 25 °C using an ALV/DLS/ SLS-5000F, SP-86 goniometer system (ALV-GmbH, Langen, Germany) equipped with a CW diode-pumped

Nd:YAG solid-state Compass-DPSS laser with a symmetrizer (Coherent Inc., Santa Clara, CA). The laser operates at 532 nm with an output power of 400 mW. The intensity scale was calibrated against scattering from toluene. Independent 1.76 mM HEWL samples incubated at 60 °C for periods of 1 to 7 days were analyzed at least three times. Measurements were made at a scattering angle 90° to the incident beam for 5-10 min.

AFM: Independent 1.76 mM HEWL samples incubated at 60 °C for 0, 1, 2, 3, 4 and 7 days were diluted 1:400 in 25 mM HCl, pH 1.6. Samples were spin-coated onto silicon wafers and dried in vacuum conditions for 4-5 hours. AFM images were recorded in non-contact mode using an AFM, JEOL instrument (JSPM 4210) equipped with a nitride cantilever NSC15 from MicroMasch, USA. Typical working frequency and spring constant: 325 kHz and 40 N/m, respectively. Topography images were recorded adapting the offset point according to the roughness of each sample.

TEM: Independent 1.76 mM HEWL samples were incubated at 60 °C for periods of 1 to 7 days. Sample solutions were applied onto a carbon-formvar coated 200–400 mesh spacing grids. After 1 minute, excess sample solution was removed by blotting with filter paper and stained with filtered aqueous solution of 2% uranyl acetate (for 45 seconds). Grids were examined under a JEOL JEM 1400 TEM (Tokyo, Japan) operated at 80 kV. Images were digitally recorded using a Gatan SC 1000 ORIUS CCD camera (Warrendale, PA, USA).

Mathematical Model Derivation: In the presence of off-pathway aggregation, the increase of total aggregates in solution is due to the formation of either amyloid fibrils or off-pathway aggregates:

$$\frac{dm}{dt} = \frac{dm_a}{dt} + \frac{dm_{off}}{dt} \quad (3)$$

While the former process is described by the two-parameter CLM (16), the latter is here characterized by a off-pathway nucleation step, which, similar to amyloid nucleation, is considered to be second-order in relation to supersaturation:

$$\frac{dm_{off}}{dt} = k_{off}^* V \sigma_{off}^2 \quad (4)$$

The rate constant k_{off}^* is the nucleation frequency expressed per volume of solution (V). Since the two types of aggregates in question have distinct

structural organizations, the concentration of soluble protein equilibrating the solid phase is also different, i.e., supersaturation has to be differently defined as a function of the protein solubility C_i^* for amyloid fibrils (subscript $i = a$) and for off-pathway aggregates (subscript $i = off$):

$$\sigma_i = \frac{C - C_i^*}{C_i^*} \quad (5)$$

As the formation of total aggregates and the depletion of soluble protein are complementary processes, m is proportional to the difference $(C_0 - C)$ and σ_i is alternatively expressed as

$$\sigma_i = \left(1 - \frac{m}{M_i}\right) \sigma_{0,i} \quad (6)$$

where M_i is the total amount of species i (either a or off) that would be produced in the absence of the other species (either off or a), and $\sigma_{0,i}$ is the initial supersaturation i evaluated according to eq. 5 – both M_i and $\sigma_{0,i}$ are proportional to the difference $(C_0 - C_i^*)$. Accordingly, eq. 4 is rewritten as

$$\frac{dm_{off}}{dt} = k_{off}^* V \sigma_{0,off}^2 \left(1 - \frac{m}{M_{off}}\right)^2 \quad (7)$$

whereas the differential form of the CLM equation (16),

$$\frac{d\alpha_a}{dt} = k_a \frac{\sigma_a}{\sigma_{0,a}} \left(k_b \frac{\sigma_a}{\sigma_{0,a}} + \alpha_a\right) \quad (8)$$

is rewritten as

$$\frac{d\alpha_a}{dt} = k_a \left(1 - \frac{m}{M_a}\right) \left(k_b \left(1 - \frac{m}{M_a}\right) + \alpha_a\right) \quad (9)$$

where k_a is defined as the autocatalytic rate constant and k_b gives the relative rates of primary nucleation steps over autocatalytic steps. The amyloid conversion is normalized as $\alpha_a = m_a / M_a$ thus implying that the final value of 1 is only reached when no off-pathway aggregates are formed. In all other occasions the final value of α_a represents the fraction of amyloid fibrils produced in relation to that expected in the absence of a competitive process. In our simulations amyloid fibrils are not supposed to dissolve once the protein concentration decreases

below the solubility value C_a^* . After that limit, the amyloid supersaturation σ_a is considered 0. By adopting normalized units of time ($\theta = k_a t$) and of total amount of aggregates ($\beta = m / M_0$) on eq. 9 results:

$$\frac{d\alpha_a}{d\theta} = \left(1 - \beta \frac{M_0}{M_a}\right) \left(k_b \left(1 - \beta \frac{M_0}{M_a}\right) + \alpha_a\right) \quad (10)$$

The same procedure is applied to eq. 4, which is finally replaced in eq. 3 to obtain

$$\frac{d\beta}{d\theta} = \frac{M_a}{M_0} \left(1 - \beta \frac{M_0}{M_a}\right) \left(k_b \left(1 - \beta \frac{M_0}{M_a}\right) + \alpha_a\right) + k_{off} \left(1 - \beta \frac{M_0}{M_{off}}\right)^2 \quad (11)$$

where k_{off} is the normalized rate constant for off-pathway aggregation,

$$k_{off} = \frac{k_{off}^* V \sigma_{0,off}^2}{k_a M_0} \quad (12)$$

and M_0 is the final amount of total aggregates. Being proportional to C_0 minus the final concentration of soluble protein (either C_a^* or C_{off}^*), M_0 also corresponds to either M_a or M_{off} depending on which species – amyloid fibrils or off-pathway aggregates – dictates the equilibrium.

The system of ordinary differential equations formed by eqs. 10 and 11 was solved using Matlab® subject to the initial conditions $\alpha_a(0) = 0$ and $\beta(0) = 0$, and according to the details given in each of the following numerical simulations.

Simulation 1–Effect of the off-pathway rate constant k_{off} on the aggregation kinetics: We have solved eqs. 10 and 11 for different combinations of parameters k_b and k_{off} . The used value of M_0 / M_a was estimated based on measurements of $C_a^* = 1.50$ mM and $C_{off}^* = 0.75$ mM obtained during protein depletion experiments carried out at $C_0 = 1.76$ mM:

$$\frac{M_0}{M_a} = \frac{C_0 - C_{off}^*}{C_0 - C_a^*} \quad (13)$$

Since off-pathway aggregates have the lowest solubility, the final amount of total aggregates M_0 is calculated using C_{off}^* as the equilibrium protein concentration and $M_0/M_{off} = 1$.

Simulation 2–Effect of the initial protein concentration C_0 on the aggregation kinetics: Equations 10 and 11 were also solved taking into account C_0 -dependent variables M_0/M_a (eq. 13), k_b (proportional to $\sigma_{0,a}$) and k_{off} , whose definition can be rewritten as

$$k_{off} = \frac{k_{off}^*}{M_w \kappa} \left(\frac{\sigma_{0,off}}{\sigma_{0,a}} \right) \quad (14)$$

obtained after replacing in eq. 12 (i) the direct dependence of k_a on $\sigma_{0,a}$,

$$k_a = \kappa \sigma_{0,a} \quad (15)$$

and (ii) the definition of M_0 ,

$$M_0 = (C_0 - C_{off}^*) M_w V \quad (16)$$

with M_w being the molecular weight of the amyloidogenic protein. From the obtained $\alpha_a(\theta)$ progress curves we computed the corresponding $\alpha(\theta)$ curves following the definitions given in Simulation 1. The theoretical half-life coordinates t_{50} and v_{50} were respectively obtained from the normalized time required to reach 50% conversion θ_{50} and from slope $d\alpha/d\theta$ at the same instant:

$$t_{50} = \frac{\theta_{50}}{\kappa \sigma_{0,a}} \quad (17)$$

$$v_{50} = \kappa \sigma_{0,a} \left. \frac{d\alpha}{d\theta} \right|_{50} \quad (18)$$

As arbitrary units of time and aggregation rate are used, an arbitrary value of κ is also considered. The influence of C_0 on $\sigma_{0,a}$ and $\sigma_{0,off}$ in eqs. 14, 17 and 18 is given in eq. 5. Different solutions were obtained for different values of C_0 , $k_b/\sigma_{0,a}$ and $k_{off} \sigma_{0,a}/\sigma_{0,off}$.

RESULTS

The amyloid fibrillization curves of HEWL suggest off-pathway aggregation (OPA): The comparative analysis made in Introduction indicates that the CLM can be used as a touchstone to identify and

characterize unconventional aggregation kinetics. This is now illustrated using *in vitro* experimental data measured by us during the aggregation of HEWL under conditions of low pH (1.6), high temperature (60 °C) and high HEWL concentration (≥ 0.60 mM) required to produce amyloid fibrils without added denaturants or salts. Representing the results as the normalized intensity of ThT fluorescence with time (Fig. 2a) and by the concentration-dependent half-life coordinates (Figs. 2b and 2c) does not seem to indicate especially unusual kinetics, except the weak concentration dependence of t_{50} (Fig. 2b) and v_{50} (Fig. 2c). Characteristic but not exclusive of HEWL aggregation, the low reproducibility of the results further prevents definitive conclusions to be taken without testing wider ranges of protein concentrations and numerous other replicates (40,43,47,48). The previously reported formation of intermediate and off-pathway species during amyloid fibrillization of lysozyme should however produce atypical kinetic signatures and explain in part the poor reproducibility indexes. Parallel phase transition processes, such as the formation of insoluble oligomers and protein precipitates, acts as a sink of the soluble amyloid pool thus affecting the rate at which amyloid fibrils are formed and their final amount. Since the non-amyloidogenic pathways also involve stochastic nucleation steps, their presence is expected to increase the overall variability of the results.

The impact of an additional source of monomer depletion besides primary nucleation, secondary nucleation and fibril elongation was investigated within the CLM framework by introducing an off-pathway nucleation step, which, similar to amyloid nucleation, is considered to be second-order in relation to supersaturation. From this theoretical exercise, which is described in detail in Experimental Procedures, we found practical ways to identify supplementary kinetic steps from a single aggregation curve (Figs. 3 and 4); as shown in Figure 3a, the conventional hyperbolic/sigmoidal curves previously represented in Figure 1a are expected to show a noticeable linear phase when amyloid conversion is expressed as $\alpha/(1-\alpha)$ and represented as a function of time in a log-linear scale. Note that $\alpha/(1-\alpha)$ corresponds to the mass of fibrils

already produced divided by the mass of fibrils still to be formed. The linear phase starts after elapsed a period of time of $\approx k_a^{-1}$ and lasts until the end of the reaction. In the case of sigmoidal curves (low k_b values in Fig. 3a), this interval should include the whole fast growth period. As a first fingerprint of the presence of off-pathway species, a disturbance to the linear profile is shown in Figure 3b with the initial concave phase being prolonged until later stages of amyloid fibril formation. As the amyloid reaction approaches completion, the concave phase is immediately succeeded by a convex phase, whose presence might be difficult to identify in practice due to the increased signal noise of $\alpha/(1-\alpha)$ data. As Figures 4e and 4f also show, the deviations from linearity result from the existence of a parallel nucleation step characterized by the rate constant k_{off} . Representing the measured HEWL aggregation curves in the modified coordinates consistently show nonlinear concave trends during the fast growth stages - Figure 3c. Owing to fluorescence noise amplification, the initial and final reaction stages are omitted in Figure 3c. Log-linear representations of the measured $\alpha/(1-\alpha)$ with the incubation time are a new probe for the presence of off-pathway aggregates with facile implementation during high-throughput inhibitor screenings. However, and as discussed next, the information provided by representations such as Figure 3c is essentially qualitative and requires additional scaling studies in order to be consolidated.

Ideal curves with marked linear phases as in Figure 3a do not necessarily mean the absence of supplementary pathways, which might take place at much slower rates than amyloid fibrillization. On the other hand, prolonged concave phases eventually followed by a convex phase (Figs. 3b, 3c, and Figs. 4e and 4f) are a necessary but not sufficient condition for the existence of parallel phase transition processes, seeing that similar outcomes might be produced by other phenomena, e.g., fluorescence quenching. The results obtained from Simulation 1 (Experimental Procedures) and represented in Figures 4a and 4b suggest additional evidences based on the variability of the endpoint signals F_∞ . In principle, these thermodynamically determined measurements

should be highly reproducible since they are not subject to stochastic contingencies as, for example, the nucleation steps. Figures 4a and 4b show, however, that the endpoint signals are expected to change as different values of k_b and k_{off} are considered. This is understandable in view of the existing competition between amyloid and off-pathway nucleation: the faster is one process relatively to the other, the larger is its share of the total soluble protein. In turn, if no OPA takes place, it does not matter thermodynamically whether amyloid formation is fast or slow, reproducible or changeable, because the value of F_∞ is mainly determined by the $(C_0 - C_a^*)$ difference. The experimental results previously shown in Figure 2a are associated to highly variable end-point fluorescence signals (data not shown). Such low reproducibility is normally associated to the nucleation rate constant k_b due to the exponentiation of the lag-time variability (16). The propagation of the kinetic uncertainty to the F_∞ values can be justified by the occurrence of parallel nucleation processes, both characterized by fluctuating rate constants (k_b and k_{off}).

OPA Scaling Laws: After having scrutinized the progress curves of HEWL aggregation subject to different types of normalization and having analyzed the variability of the endpoint fluorescence signal, it remains to be discussed the peculiar scaling laws of t_{50} and v_{50} with protein concentration. In fact, the exponent γ determined from the results in Figure 2b, and the aggregation rate data represented in Figure 2c are indicative of abnormally weak influence of C_0 on the two half-life coordinates. When only amyloid fibrils are formed, minimum values of $|\gamma| \approx 1$ are predicted by the CLM under conditions of low nucleation rates (Fig. 1b), for which v_{50} also reduces to $\approx 4k_a$, a linear function of C_0 (16). The measured relationships shown in Figures 2b and 2c are unexpected not only by the 2-parameter CLM as by any other current model (see discussion of Fig. 1). Once again a solution to this problem seems possible by extending CLM to account the formation of non-amyloidogenic precipitates. The altered role of the initial protein concentration is studied in Simulation 2 (Experimental

Procedures), with Figure 5 showing the numerical solutions assuming predominant OPA ($k_b/k_{off} \ll 1$). Figure 5a shows that the duration of the lag phase hardly changes with the protein concentration ($\gamma \simeq 0$) and that t_{50} may even increase with C_0 ($\gamma > 0$). This apparently contradictory result is explained by the presence of a competitive off-pathway step that is comparatively more favored by higher C_0 values than the amyloid aggregation step. Equally, Figure 5b shows that the amyloid aggregation rate v_{50} can be weakly influenced by C_0 or even decrease as C_0 increases. To be observed, these paradoxical kinetic results require high values of k_{off} in order that the considered range of protein concentration is above the critical limit for amyloid formation. Figure 5 also shows sudden variations of the $t_{50}(C_0)$ and $v_{50}(C_0)$ scaling factors taking place along narrow ranges of C_0 values. In agreement with estimations of γ taken from literature (40), the broken curves are not confined to protein concentrations close to the amyloid solubility (as in Fig. 1b) but can be observed for C_0/C_a^* values $\gg 1$. Our selection of k_b and k_{off} values in Figure 5 places the region of weak C_0 dependencies in the same C_0/C_a^* range as that used during the HEWL aggregation experiments. While reconciling the results of Figures 2b and 2c with the theory of protein aggregation, this agreement is the first step towards a univocal, all-inclusive validation of the model of which the following section presents a numerical attempt.

Protein depletion confirms OPA prevalence: At this point, we have accumulated a set of evidences suggesting that amyloid fibrils are only the tip of an iceberg hiding a crowd of ThT-invisible aggregates. Although independent from each other, these evidences stem, in all cases, from conventional ThT fluorescence measurements. The first estimations of k_b values $\sim 10^{-7}$, indicate that the amyloid nucleation is many order of magnitudes slower than the autocatalytic steps. On the other hand, k_{off} values comprised between $\sim 10^{-2}$ and $\sim 10^{-1}$ configure a case where off-pathway species are produced at much higher rates

than amyloid fibrils. These conclusions were further tested by complementary techniques, namely, by checking whether the depletion of protein from solution matches the observed kinetics of amyloid fibril formation (Figs. 6a and 6b). By changing the focus from the amyloid fibrils to the dissolved protein we also wanted to measure the equilibrium concentration for long reaction times as an estimation of the thermodynamic solubility. Independent HEWL samples incubated at the same conditions of pH and temperature as during the fluorimetric assays were periodically filtered and analyzed spectrophotometrically at 280 nm (see Materials and Methods). The results in Figure 6a show that solute depletion starts immediately after incubation, i.e., before the formation of any detectable amount of amyloid fibrils (Fig. 6b); moreover, phase transition processes continue to occur many days after the plateau in fluorescence emission is reached. Besides confirming the predominance of OPA, these results also indicate that HEWL amyloid fibrils equilibrate with the solution earlier, and at higher protein concentration, than the other aggregates. The simulated curves in Figure 6a were computed using the estimates of k_b and k_{off} that followed from ThT fluorescence kinetic analysis and using the values of amyloid solubility (C_a^*) and off-pathway solubility (C_{off}^*) of 1.50 mM and 0.75 mM corresponding to estimations of HEWL concentration after ~ 90 h and $\gg 1000$ h incubation, respectively. The calculated dimensionless time needed to obtain the same total conversion as after 700 h incubation was $k_a t = 100$, from which the value of $k_a = 1/7 \text{ h}^{-1}$ was determined. The good agreement between simulated and measured results reported in Figure 6a was achieved using a relatively narrow range of k_{off} values (color bar), meaning that the expectable variability of this parameter is able to explain the observed scattering of the measured profile. Despite all the converging evidences, the set of values chosen for k_a , k_b and k_{off} should be taken as approximate guesses rather than as definitive results. This is because the adopted equilibrium concentrations for amyloid (C_a^*) and off-pathway (C_{off}^*)

aggregates are expected to differ substantially from the real thermodynamic solubilities. Not only the solutions are highly concentrated and nonideal, but also the chemical potential of the solute seems to be drastically influenced by the presence of aggregates in a process akin to volume exclusion effects (49). The asymptotic HEWL concentration of 0.75 mM estimated for long reaction times implies that aggregation assays conducted at concentrations below this limit would not produce off-pathway precipitates, let alone amyloid fibrils. Yet, as the results in Figure 2 demonstrate, HEWL concentrations as low as 0.60 mM continue to produce aggregates that stain positive for ThT. The thermodynamic concentration of dissolved protein seems to be decreased by the presence of aggregates, which, combined with changes in solution viscosity may explain why the phase transition processes cease at high HEWL concentrations and high content of total aggregates. These effects, to be discussed in detail elsewhere, imply a faster supersaturation decrease than that considered in our model. Therefore, they should also account for the differences observed in Figure 6b where the measured aggregation curves move faster towards equilibrium than the expected by the extended CLM for the selected set of parameters. Using real protein concentrations in our theoretical simulations would require time-evolving activity coefficients that are not available right now.

Complementary structural, morphological and size-distribution data: The changes in the secondary structure of HEWL were followed by recording the far-UV spectra along the different phases of the aggregation process (Fig. 6c). The far-UV spectrum of non-incubated HEWL shows the 208 nm and 222 nm bands characteristic of the α -helical structure of the native protein (50). Upon the first day of incubation, the ellipticity strongly decreases and the minimum CD intensity takes place at slightly lower wavelengths. The same tendency is observed until day 4, yet with smaller variations of CD. These results indicate the formation of pre-amyloid structures, presumably amorphous aggregates, which are less helical than the initial conformation. The formation of ThT-positive aggregates after the first day of incubation (Fig. 6b) did not provoke the position of minimum CD to clearly deviate from ~ 208 nm to ~ 215 – 220 nm as expected for β -sheet structures. Therefore,

and as suggested by the protein depletion results, amorphous aggregation seems to prevail over amyloid fibrillization since the beginning of incubation. The CD intensity continues to decrease from day 4 to 7 as a consequence of the formation of off-pathway aggregates and the increased number and size of scattering objects in solution (19). No amyloid fibrils are formed during this period as indicated by the ThT fluorescence plateau in Figure 6b.

To gain insight into the size and morphology of the aggregates present in solution, samples incubated for different time periods were further analyzed using DLS and Atomic Force Microscopy (AFM) – Figure 7. The size distributions obtained from scattered light intensity measurements reveal how the populations of soluble protein and insoluble aggregates evolve with time (Fig. 7a). The relative weight of the peak centered near a hydrodynamic radius R_h of 2 nm is an indirect estimate of the amount of soluble HEWL. As shown in the inset of Figure 7a, the variation of this fraction during the incubation time resembles that of protein concentration measured by UV absorption in Figure 6a. This is another independent verification that phase transition processes occur before and after amyloid fibril formation. Even though particles with R_h greater than 50 nm are identified before incubation at 60 °C, the first DLS dataset is not sufficiently resolved to distinguish between the different pre-aggregation species. As the incubation starts, the distribution of particles centered near 70 nm becomes better defined simultaneously with the formation of the amorphous aggregates. Coinciding with the period of fast ThT fluorescence increase (Fig. 6b), a third peak centered near ~ 500 nm emerges at the end of day 2 as the likely result of the formation of mature amyloid fibrils. After that, the two aggregate peaks become blended in a single distribution centered in a hydrodynamic radius still close to 100 nm but with the right tail exceeding the submicron range. Since the scattering intensity of a particle is proportional to the sixth power of its diameter, the results in Figure 7a suggest the existence of a population of amorphous aggregates with mean R_h of 70 nm dominating over a second population of greater R_h , presumably mature amyloid fibrils, having a widely dispersed size distribution owing in part to fibril breakage. Given

the limitations of DLS to morphologically describe less prevalent, non-spherical particles (51), the amyloidogenic samples were also characterized using AFM and Transmission Electron Microscopy (TEM). The selected AFM image in Figure 7b confirms that 1.76 mM HEWL solutions at pH 1.6 already contain amorphous aggregates before incubation at 60 °C. Present in all analyzed samples, these precipitates generally have the shape of a disk with height ~5 nm and diameter within the range 20-150 nm also obtained for R_h in Figure 7a. Figure 8 shows the results of further examinations using TEM, with small worm-like aggregates being identified in Figures 8b and 8e. It remains unclear whether these protofibrils twist over themselves to form disk-shaped aggregates or continue to develop to form amyloid fibrils. In Figure 7c we surprisingly identified the presence of mature amyloid fibrils as long as 2 μ m and ~10 nm diameter at the end of the first day of incubation. Despite their size, these fibrils are scarce enough to remain undetected during ThT fluorescence and DLS measurements. Therefore, amyloid fibrils seem to grow much faster than they are nucleated in agreement with the low value estimated for parameter k_b ($\sim 10^{-7}$). The AFM images in Figures 7d and 7e show well differentiated curvilinear fibrils, whereas the TEM images additionally report straighter fibrils generally surrounded by amorphous aggregates – see Figures 8e-f. These variations are the likely result of different sample handling, which in the case of AFM involved 1:400 dilution and spin-coated deposition onto silicon wafers.

DISCUSSION

Similarly to other phase transition phenomena, amyloid fibril formation takes place via a nucleation and growth mechanism until thermodynamic equilibrium is reached. The amyloid pathway may however comprise parallel steps and intermediate species that are no less relevant for the development of amyloidosis and neurodegenerative diseases than the deposition of fibrils itself. Protein aggregation curves measured *in vitro* using amyloid-specific dyes are shown to provide much more information about OPA than what is conventionally extracted. The set of canonical behaviors summarized in Figure 1 can be expected when off-pathway species are either

absent or present in minor amounts. Even if some of those kinetic results are not predicted by established theories, they are in conformity with the classical mechanism involving primary nucleation and auto-catalytic steps. The CLM was extended to include a third rate constant (k_{off}) characterizing the parallel nucleation step. The numerical solutions of the three-parameter CLM unveil the kinetic signatures characteristic of OPA; these include non-linear variation of $\alpha/(1-\alpha)$ with time when plotted in a log-linear scale, highly variable endpoint signals, values of the t_{50} absolute scaling factor $|\gamma|$ below 1 and sublinear increase of v_{50} with the protein concentration. In cases of extensive OPA, increasing the protein concentration may even prolong the duration of the lag phase and decrease the amyloid aggregation rate. This angle of approach is, to our knowledge, totally original as the main focus has been on the detection and morphological/toxicological characterization of the amorphous precipitates (4,7,8,9,14). The new possibility of estimating the relative amounts of off-pathway and amyloid aggregates accentuates the need for cataloguing the deleterious species in each disease. After deciding what aspect of protein aggregation one wants to target, extensive screenings of off-pathway modulators can from now on be routinely implemented.

As a proof-of-concept the modified CLM was tested against ThT aggregation data of HEWL measured under conditions of low pH (1.6) and high temperature (60 °C) known to produce off-pathway aggregates. The estimated values of k_a , k_b and k_{off} suggest that off-pathway species are produced much earlier and at higher rates than amyloid fibrils, which, nevertheless, rapidly reach their mature size once the stable nucleus is formed. This was supported by complementary analysis of soluble protein depletion with time, far-UV CD spectra, particle size distributions measured using DLS and aggregates morphology observed using AFM and TEM. We further concluded that amorphous aggregates generally have the shape of a disk with diameters comprised between 20 and 150 nm, even though small worm-like aggregates were also identified. Amyloid fibrils with 10 nm diameter are consistently longer

than 1 μm and show a broad size distribution as a likely consequence of fibril breakage.

While offering an explanation for puzzling kinetic behaviors, our study contributes to a better understanding of the molecular basis of amyloid diseases and is expected to find practical application in neurodegenerative drug research. By using the analytical probes for OPA here proposed, libraries of small molecule compounds can be screened targeting the formation of amorphous aggregates without any additional

means being required besides the current amyloid-specific markers and high-throughput methods. Whether the kinetic signatures are attenuated or intensified by the screened molecules provides a valuable indication of their potential as off-pathway modulators. This therapeutic strategy aims at inhibiting or promoting OPA according to the disruptive or stabilizing effect that non-fibrillar species may have on the regulatory mechanisms during disease.

Acknowledgments – R.C. gratefully acknowledges grant no. SFRH/BD/74174/2010 from Fundação para a Ciência e a Tecnologia (FCT), Portugal. P.T. thanks Ministerio de Economía y Competitividad (MINECO) and Xunta de Galicia for research projects MAT 2013-40971-R and EM2013-046, respectively. E.V.A. is grateful to the Spanish Ministerio de Economía y Competitividad for her FPU (AP2012-2921) fellowship. Two of the authors (P.T. and P.M.M.) acknowledge the European Union's mobility grants Iacobus Programme and Erasmus+ Programme.

Conflict of interest – The authors declare that they have no conflicts of interest with the contents of this article.

Author Contributions – R.C., E.V.A, P.T. and P.M.M. performed the experiment and analyzed the data. R.C., P.T., F.A.R., A.M.D. and P.M.M. conceived and designed the experimental approach. P.M.M. developed the theoretical model. R.C., P.T., F.A.R., A.M.D. and P.M.M. wrote the manuscript.

REFERENCES

1. Kulmala, M., Kontkanen, J., Junninen, H., Lehtipalo, K., Manninen, H. E., Nieminen, T., Petäjä, T., Sipilä, M., Schobesberger, S., and Rantala, P. (2013) Direct observations of atmospheric aerosol nucleation. *Science* **339**, 943-946
2. Kollman, J. M., Merdes, A., Mourey, L., and Agard, D. A. (2011) Microtubule nucleation by γ -tubulin complexes. *Nat. Rev. Mol. Cell Biol.* **12**, 709-721
3. Wang, Y., Azaïs, T., Robin, M., Vallée, A., Catania, C., Legriel, P., Pehau-Arnaudet, G., Babonneau, F., Giraud-Guille, M.-M., and Nassif, N. (2012) The predominant role of collagen in the nucleation, growth, structure and orientation of bone apatite. *Nat. Mater.* **11**, 724-733
4. Glabe, C. G. (2008) Structural classification of toxic amyloid oligomers. *J. Biol. Chem.* **283**, 29639-29643
5. Uversky, V. N., and Fink, A. L. (2004) Conformational constraints for amyloid fibrillation: the importance of being unfolded. *Biochim. Biophys. Acta, Proteins Proteomics* **1698**, 131-153
6. Adachi, M., So, M., Sakurai, K., Kardos, J., and Goto, Y. (2015) Supersaturation-limited and unlimited phase transitions compete to produce the pathway complexity in amyloid fibrillation. *J. Biol. Chem.* **290**, 18134-18145
7. Krishnan, R., Goodman, J. L., Mukhopadhyay, S., Pacheco, C. D., Lemke, E. A., Deniz, A. A., and Lindquist, S. (2012) Conserved features of intermediates in amyloid assembly determine their benign or toxic states. *Proc. Natl. Acad. Sci. U.S.A.* **109**, 11172-11177
8. Bieschke, J., Herbst, M., Wiglenda, T., Friedrich, R. P., Boeddrich, A., Schiele, F., Kleckers, D., del Amo, J. M. L., Grüning, B. A., and Wang, Q. (2012) Small-molecule conversion of toxic oligomers to nontoxic β -sheet-rich amyloid fibrils. *Nat. Chem. Biol.* **8**, 93-101
9. Hopping, G., Kellock, J., Barnwal, R. P., Law, P., Bryers, J., Varani, G., Caughey, B., and Daggett, V. (2014) Designed α -sheet peptides inhibit amyloid formation by targeting toxic oligomers. **3**

10. Ehrnhoefer, D. E., Bieschke, J., Boeddrich, A., Herbst, M., Masino, L., Lurz, R., Engemann, S., Pastore, A., and Wanker, E. E. (2008) EGCG redirects amyloidogenic polypeptides into unstructured, off-pathway oligomers. *PLoS One* **15**, 558-566
11. Hall, D., Kardos, J., Edskes, H., Carver, J. A., and Goto, Y. (2015) A multi-pathway perspective on protein aggregation: Implications for control of the rate and extent of amyloid formation. *FEBS Lett.* **589**, 672-679
12. Lee, J., Culyba, E. K., Powers, E. T., and Kelly, J. W. (2011) Amyloid- β forms fibrils by nucleated conformational conversion of oligomers. *Nat. Chem. Biol.* **7**, 602-609
13. Wetzel, R. (2006) Kinetics and thermodynamics of amyloid fibril assembly. *Acc. Chem. Res.* **39**, 671-679
14. Ruggeri, F., Longo, G., Faggiano, S., Lipiec, E., Pastore, A., and Dietler, G. (2015) Infrared nanospectroscopy characterization of oligomeric and fibrillar aggregates during amyloid formation. *Nat. Commun.* **6**
15. Gillam, J., and MacPhee, C. (2013) Modelling amyloid fibril formation kinetics: mechanisms of nucleation and growth. *J. Phys. Condens. Matter* **25**, 373101
16. Crespo, R., Rocha, F. A., Damas, A. M., and Martins, P. M. (2012) A generic crystallization-like model that describes the kinetics of amyloid fibril formation. *J. Biol. Chem.* **287**, 30585-30594
17. Martins, P. M. (2013) True and apparent inhibition of amyloid fibril formation. *Prion* **7**, 136-139
18. Morris, A. M., Watzky, M. A., and Finke, R. G. (2009) Protein aggregation kinetics, mechanism, and curve-fitting: a review of the literature. *Biochim. Biophys. Acta, Proteins Proteomics* **1794**, 375-397
19. Juárez, J., Taboada, P., and Mosquera, V. (2009) Existence of different structural intermediates on the fibrillation pathway of human serum albumin. *Biophys. J.* **96**, 2353-2370
20. Holm, N. K., Jespersen, S. K., Thomassen, L. V., Wolff, T. Y., Sehgal, P., Thomsen, L. A., Christiansen, G., Andersen, C. B., Knudsen, A. D., and Otzen, D. E. (2007) Aggregation and fibrillation of bovine serum albumin. *Biochim. Biophys. Acta, Proteins Proteomics* **1774**, 1128-1138
21. Hurshman, A. R., White, J. T., Powers, E. T., and Kelly, J. W. (2004) Transthyretin aggregation under partially denaturing conditions is a downhill polymerization. *Biochemistry* **43**, 7365-7381
22. Faria, T. Q., Almeida, Z. L., Cruz, P. F., Jesus, C. S., Castanheira, P., and Brito, R. M. (2015) A look into amyloid formation by transthyretin: aggregation pathway and a novel kinetic model. *Phys. Chem. Chem. Phys.* **17**, 7255-7263
23. Chatani, E., Yagi, H., Naiki, H., and Goto, Y. (2012) Polymorphism of β 2-microglobulin amyloid fibrils manifested by ultrasonication-enhanced fibril formation in trifluoroethanol. *J. Biol. Chem.* **287**, 22827-22837
24. Ramachandran, G., and Udgaonkar, J. B. (2011) Understanding the Kinetic Roles of the Inducer Heparin and of Rod-like Protofibrils during Amyloid Fibril Formation by Tau Protein. *J. Biol. Chem.* **286**, 38948-38959
25. Yang, S., Griffin, M. D., Binger, K. J., Schuck, P., and Howlett, G. J. (2012) An equilibrium model for linear and closed-loop amyloid fibril formation. *J. Mol. Biol.* **421**, 364-377
26. O'Nuallain, B., Freir, D. B., Nicoll, A. J., Risse, E., Ferguson, N., Herron, C. E., Collinge, J., and Walsh, D. M. (2010) Amyloid β -protein dimers rapidly form stable synaptotoxic protofibrils. *J. Neurosci.* **30**, 14411-14419
27. Rangachari, V., Moore, B. D., Reed, D. K., Sonoda, L. K., Bridges, A. W., Conboy, E., Hartigan, D., and Rosenberry, T. L. (2007) Amyloid- β (1-42) rapidly forms protofibrils and oligomers by distinct pathways in low concentrations of sodium dodecylsulfate. *Biochemistry* **46**, 12451-12462
28. Gibson, T. J., and Murphy, R. M. (2006) Inhibition of insulin fibrillogenesis with targeted peptides. *Protein Sci.* **15**, 1133-1141
29. Oosawa, F., and Kasai, M. (1962) A theory of linear and helical aggregations of macromolecules. *J. Mol. Biol.* **4**, 10-21
30. Ferrone, F. (1999) [17] Analysis of protein aggregation kinetics. *Meth. Enzymol.* **309**, 256-274

31. Knowles, T. P., Waudby, C. A., Devlin, G. L., Cohen, S. I., Aguzzi, A., Vendruscolo, M., Terentjev, E. M., Welland, M. E., and Dobson, C. M. (2009) An analytical solution to the kinetics of breakable filament assembly. *Science* **326**, 1533-1537
32. Cohen, S. I., Linse, S., Luheshi, L. M., Hellstrand, E., White, D. A., Rajah, L., Otzen, D. E., Vendruscolo, M., Dobson, C. M., and Knowles, T. P. (2013) Proliferation of amyloid- β 42 aggregates occurs through a secondary nucleation mechanism. *Proc. Natl. Acad. Sci. U.S.A.* **110**, 9758-9763
33. Yoshimura, Y., Lin, Y., Yagi, H., Lee, Y.-H., Kitayama, H., Sakurai, K., So, M., Ogi, H., Naiki, H., and Goto, Y. (2012) Distinguishing crystal-like amyloid fibrils and glass-like amorphous aggregates from their kinetics of formation. *Proc. Natl. Acad. Sci. U.S.A.*
34. Ciryam, P., Kundra, R., Morimoto, R. I., Dobson, C. M., and Vendruscolo, M. (2015) Supersaturation is a major driving force for protein aggregation in neurodegenerative diseases. *Trends Pharmacol. Sci.* **36**, 72-77
35. Ikenoue, T., Lee, Y.-H., Kardos, J., Yagi, H., Ikegami, T., Naiki, H., and Goto, Y. (2014) Heat of supersaturation-limited amyloid burst directly monitored by isothermal titration calorimetry. *Proc. Natl. Acad. Sci. U.S.A.* **111**, 6654-6659
36. Muta, H., Lee, Y.-H., Kardos, J., Lin, Y., Yagi, H., and Goto, Y. (2014) Supersaturation-limited amyloid fibrillation of insulin revealed by ultrasonication. *J. Biol. Chem.* **289**, 18228-18238
37. Yagi, H., Abe, Y., Takayanagi, N., and Goto, Y. (2014) Elongation of amyloid fibrils through lateral binding of monomers revealed by total internal reflection fluorescence microscopy. *Biochim. Biophys. Acta, Proteins Proteomics* **1844**, 1881-1888
38. Mulaj, M., Foley, J., and Muschol, M. (2014) Amyloid Oligomers and Protofibrils, but Not Filaments, Self-Replicate from Native Lysozyme. *J. Am. Chem. Soc.* **136**, 8947-8956
39. Jarrett, J. T., and Lansbury, P. T. (1993) Seeding "one-dimensional crystallization" of amyloid: a pathogenic mechanism in Alzheimer's disease and scrapie? *Cell* **73**, 1055-1058
40. Eden, K., Morris, R., Gillam, J., MacPhee, C. E., and Allen, R. J. (2015) Competition between Primary Nucleation and Autocatalysis in Amyloid Fibril Self-Assembly. *Biophys. J.* **108**, 632-643
41. Cohen, S. I. A., Vendruscolo, M., Welland, M. E., Dobson, C. M., Terentjev, E. M., and Knowles, T. P. J. (2011) Nucleated polymerization with secondary pathways. I. Time evolution of the principal moments. *J. Chem. Phys* **135**, 065105
42. Morris, R. J., Eden, K., Yarwood, R., Jourdain, L., Allen, R. J., and MacPhee, C. E. (2013) Mechanistic and environmental control of the prevalence and lifetime of amyloid oligomers. *Nat. Commun.* **4**, 1891
43. Brender, J. R., Krishnamoorthy, J., Sciacca, M. F. M., Vivekanandan, S., D'Urso, L., Chen, J., La Rosa, C., and Ramamoorthy, A. (2015) Probing the Sources of the Apparent Irreproducibility of Amyloid Formation: Drastic Changes in Kinetics and a Switch in Mechanism due to Micelle-Like Oligomer Formation at Critical Concentrations of IAPP. *J. Phys. Chem. B*
44. Ow, S.-Y., and Dunstan, D. E. (2013) The effect of concentration, temperature and stirring on hen egg white lysozyme amyloid formation. *Soft Matter* **9**, 9692-9701
45. Hill, S. E., Miti, T., Richmond, T., and Muschol, M. (2011) Spatial Extent of Charge Repulsion Regulates Assembly Pathways for Lysozyme Amyloid Fibrils. *PLOS ONE* **6**, e18171
46. Mishra, R., Sörgjerd, K., Nyström, S., Nordigården, A., Yu, Y.-C., and Hammarström, P. (2007) Lysozyme amyloidogenesis is accelerated by specific nicking and fragmentation but decelerated by intact protein binding and conversion. *J. Mol. Biol.* **366**, 1029-1044
47. Umemoto, A., Yagi, H., So, M., and Goto, Y. (2014) High-throughput Analysis of Ultrasonication-forced Amyloid Fibrillation Reveals the Mechanism Underlying the Large Fluctuation in the Lag Time. *J. Biol. Chem.* **289**, 27290-27299
48. Szavits-Nossan, J., Eden, K., Morris, R. J., MacPhee, C. E., Evans, M. R., and Allen, R. J. (2014) Inherent variability in the kinetics of autocatalytic protein self-assembly. *Phys. Rev. Lett.* **113**, 098101

49. Breydo, L., Reddy, K. D., Piai, A., Felli, I. C., Pierattelli, R., and Uversky, V. N. (2014) The crowd you're in with: effects of different types of crowding agents on protein aggregation. *Biochim. Biophys. Acta, Proteins Proteomics* **1844**, 346-357
50. Morshedi, D., Rezaei-Ghaleh, N., Ebrahim-Habibi, A., Ahmadian, S., and Nemat-Gorgani, M. (2007) Inhibition of amyloid fibrillation of lysozyme by indole derivatives – possible mechanism of action. *FEBS J.* **274**, 6415-6425
51. Streets, A. M., Sourigues, Y., Kopito, R. R., Melki, R., and Quake, S. R. (2013) Simultaneous measurement of amyloid fibril formation by dynamic light scattering and fluorescence reveals complex aggregation kinetics. *PLOS ONE* **8**, e54541

FOOTNOTES

¹From LEPABE, Laboratório de Engenharia de Processos, Ambiente, Biotecnologia e Energia, Departamento de Engenharia Química, Faculdade de Engenharia da Universidade do Porto. Rua Dr. Roberto Frias, 4200-465 Porto, Portugal

²Departamento de Física de la Materia Condensada, Facultad de Física, Universidad de Santiago de Compostela, Spain

³ICBAS – Instituto de Ciências Biomédicas Abel Salazar, Universidade do Porto, Porto, Portugal

The abbreviations used are: AFM, Atomic Force Microscopy; CD, Circular Dichroism; CLM, crystallization-like model; DLS, Dynamic Light Scattering; HEWL, hen egg-white lysozyme; OPA, off-pathway aggregation; SI, Supporting Information; ThT, thioflavin-T; TEM, Transmission Electron Microscopy.

FIGURE LEGENDS

FIGURE 1. Canonical kinetic profiles expected by the CLM (green and red) but not expected by other theoretical models (red). **(a)** Hyperbolic to sigmoidal protein aggregation curves are obtained from Eq. 1 as the relative magnitude of primary nucleation decreases from $k_b = 10$ to 10^{-6} (log-scale color bar). Inset: the $k_a t$ timescale is expanded to show complete sigmoidal growth curves. The hyperbolic profiles marked in red are not expected for unseeded reactions by Oosawa-type models (29,30,31). **(b)** log-log representation of t_{50} (an indicator of the duration of the lag phase) as a function of the protein concentration computed using Eq. 2 for different values of k_b/σ_0 . The slope of the dashed line corresponds to the exponential scaling factor γ (illustrative example for high protein concentrations and $k_b/\sigma_0 = 10^{-2}$). The broken curves shown in red are not expected by the different closed-form solutions of Oosawa-type and Ockham's Razor-type models. Inset: in the absence of off-pathway processes, the absolute value of γ is comprised between 1 and 2 according to the value of k_b .

FIGURE 2. Influence of the initial protein concentration on the kinetics of amyloid fibril formation of HEWL at pH 1.6 and 60 °C. **(a)** ThT fluorescence increase during the aggregation of 0.60 mM (blue), 0.93 mM (light blue), 1.25 mM (green), 1.39 mM (orange) and 1.76 mM (red) HEWL represented in normalized units as a function of the incubation time. **(b,c)** Influence of the initial HEWL concentration **(b)** on the time required to reach 50% completion (t_{50}) and **(c)** on the aggregation rate at the same instant (v_{50}). Log-log and linear-linear scales are adopted in (b) and (c), respectively; symbols and error bars represent mean values and standard deviations. **(b)** The linear fit (solid line) indicates an exponential scaling factor γ of -0.24 .

FIGURE 3. Kinetic signatures suggesting the presence of off-pathway species. **(a)** The typical CLM aggregation curves in Figure 1 (without OPA) are represented in modified log-linear coordinates relating $\alpha/(1-\alpha)$ vs. dimensionless time (same color code as in Fig. 1a). Linear relationships are observed for $k_a t > 1$ (after the lag phases in Fig. 1a are surpassed). **(b)** Effects provoked by other phase transition processes besides the nucleation and growth of amyloid fibrils. The linear phase rapidly vanishes in the presence of parallel nucleation events characterized by the rate constant k_{off} . Numerical results obtained from Simulation 1 (Experimental Procedures), using $k_b = 10^{-2}$ and the values of k_{off} indicated in the color bar. Dashed lines in (a) and (b) correspond to the same result. **(c)** The measured aggregation curves of HEWL in Figure 2a are represented in the modified coordinates (same color code as in Fig. 2a). The concave phase prolonged until amyloid conversions close to 1 suggest the existence of OPA.

FIGURE 4. Numerical solutions of the extended CLM accounting off-pathway aggregation. Equation 10 was solved as described in Simulation 1 using $k_b = 10^{-1}$ (left panel) and $k_b = 10^{-7}$ (right panel) and the values of k_{off} given in the right side color bar. Results are expressed as the variation with the normalized time $k_a t$ of (A, B) the predicted amyloid fluorescence signal F/F_a (equivalent to α_a), (C, D) the amyloid conversion α , (E, F) the modified amyloid conversion $\alpha/(1-\alpha)$ in log-linear scale and (G, H) the dimensionless amount of total aggregates m/M_0 .

FIGURE 5. Influence of the protein concentration on the half-life coordinates when OPA is predominant. Solutions of the extended CLM calculated for $k_b/\sigma_0 = 10^{-6}$ and given as **(a)** the log-log representation of t_{50} as a function of the C_0/C_a^* ratio and **(b)** the variation of v_{50} with C_0/C_a^* . **(a,b)** Different colors mean different C_0 -independent k_{off} values as indicated by the color bar in the right side. Numerical details given in Simulation 2 (Experiential Procedures).

FIGURE 6. Complementary data suggesting predominant off-pathway aggregates over amyloid fibrils. **(a)** Symbols: depletion of soluble HEWL at pH 1.6 and 60 °C with time measured by UV absorption at 280 nm after filtration through a sterile 0.22 μm filter. Lines: protein concentration decrease predicted by the extended CLM. **(b)** Amyloid fibrillization followed by ThT fluorescence (black lines) under the same conditions of pH, temperature and initial HEWL concentration (1.76 mM) as in (a). Different colored lines: same numerical solution as in **(a)** expressed as the amyloid content increase with time. HEWL depletion in (a) starts before, and continues after the formation of amyloid fibrils in (b). **(a,b)** Numerical results obtained from Simulation 2 (Experiential Procedures), using $k_a = 1/7 \text{ h}^{-1}$, $k_b = 10^{-7}$ and the range of k_{off} values indicated by the color bar in the right side; arrows: different instants of time where samples were analyzed using CD spectroscopy and DLS. **(c)** Far-UV CD spectra of HEWL samples incubated for 0, 1, 2, 3, 4 and 7 days measured at 20°C and at a 1:400 dilution. Major changes in the CD spectrum occur during the first day of incubation and from day 4 to 7, when no measurable amount of new amyloid fibrils is formed.

FIGURE 7. Aggregation of 1.76 mM HEWL at pH 1.6 and 60 °C followed by DLS and AFM. **(a)** Distribution of hydrodynamic radii R_h obtained from DLS measurements at the different instants of time marked with an arrow in Figures 6a and 6b. Inset: the relative weight of the soluble HEWL peak centered near 2 nm decreases with time. **(b-e)** Morphology of HEWL aggregates observed with AFM after **(b)** 0, **(c)** 1, **(d)** 3 and **(e)** 4 days incubation; color bar in the right side: height scale common to all AFM images.

FIGURE 8. Aggregation of 1.76 mM HEWL at pH 1.6 and 60 °C followed by Transmission Electron Microscopy. **(a-c)** Amorphous aggregates identified at the end of **(a)** 1, **(b)** 2 and **(c)** 3 days incubation; **(d-f)** amorphous aggregates and amyloid fibrils observed at the end of **(d)** 2, **(e)** 3 and **(f)** 4 days incubation. Scale bars represent 200 nm.

FIGURES
Figure 1

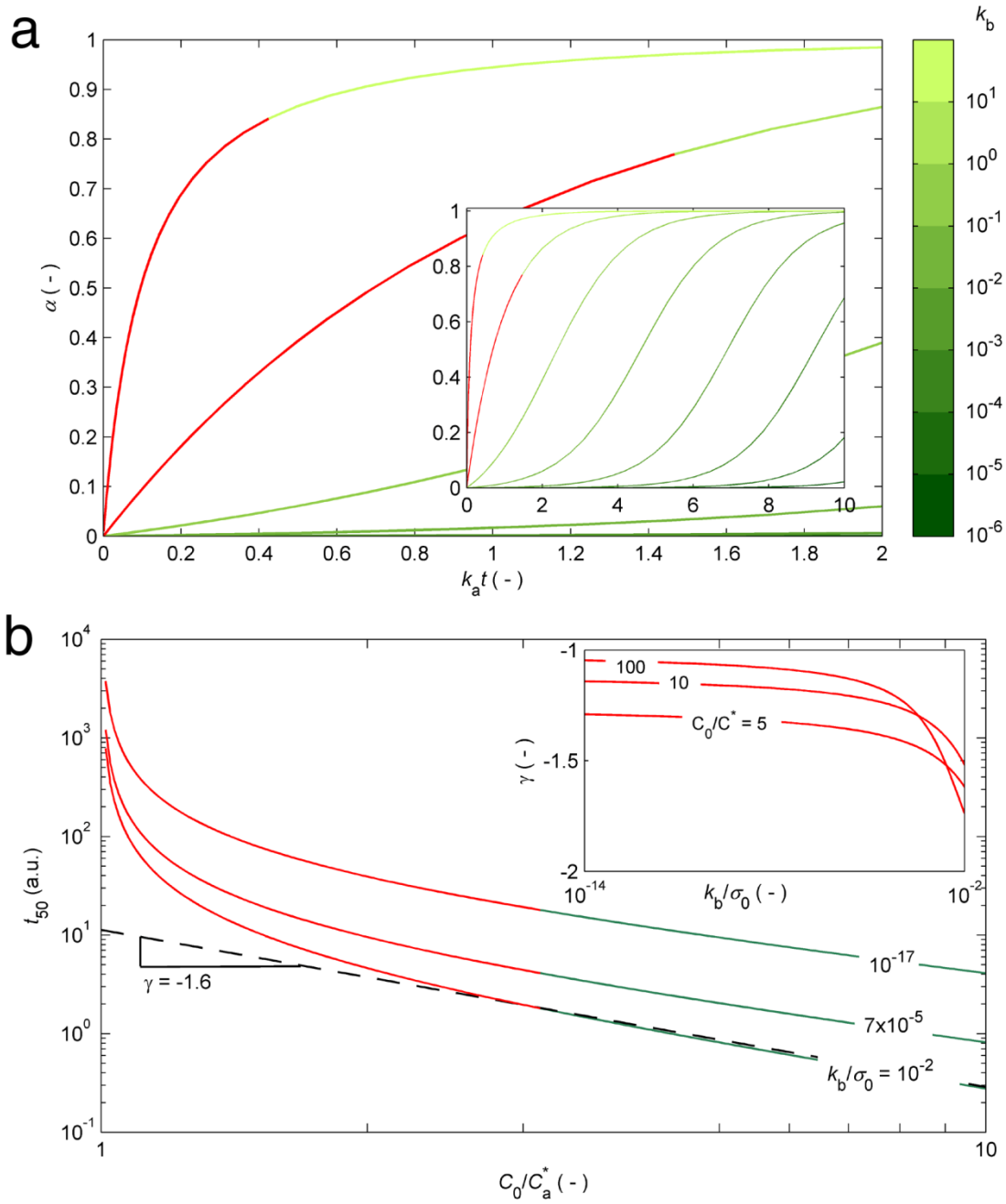


Figure 2

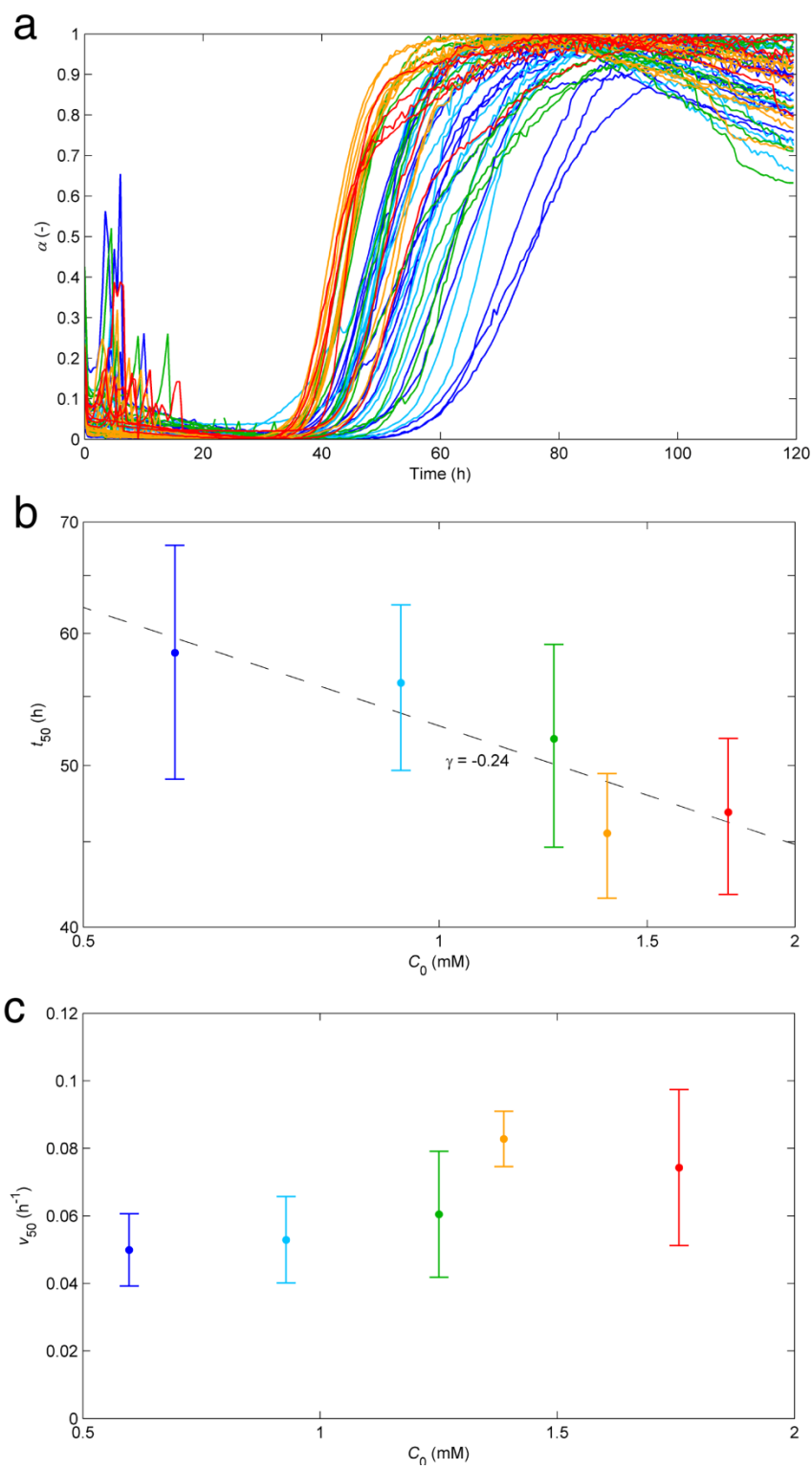


Figure 3

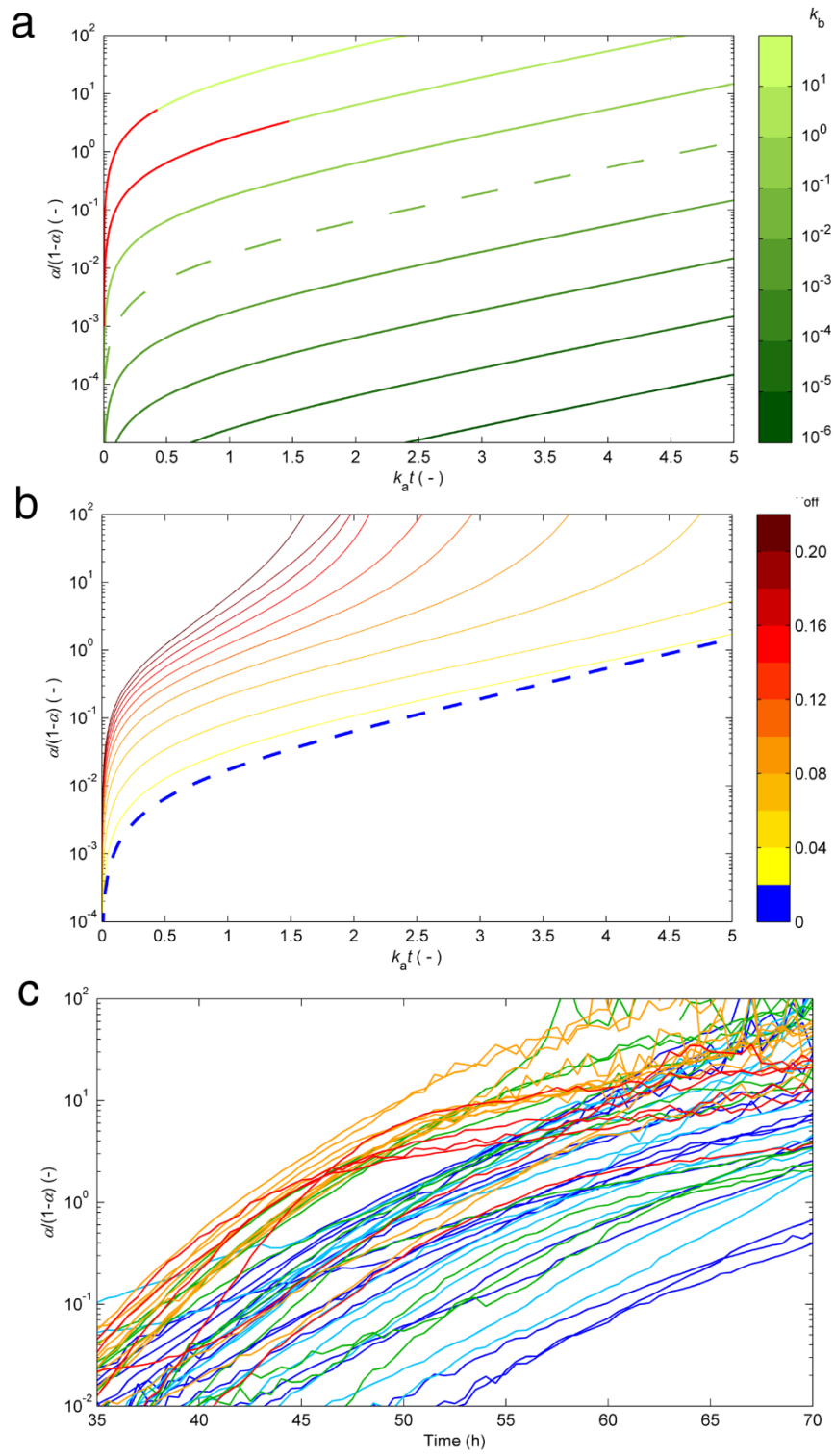


Figure 4

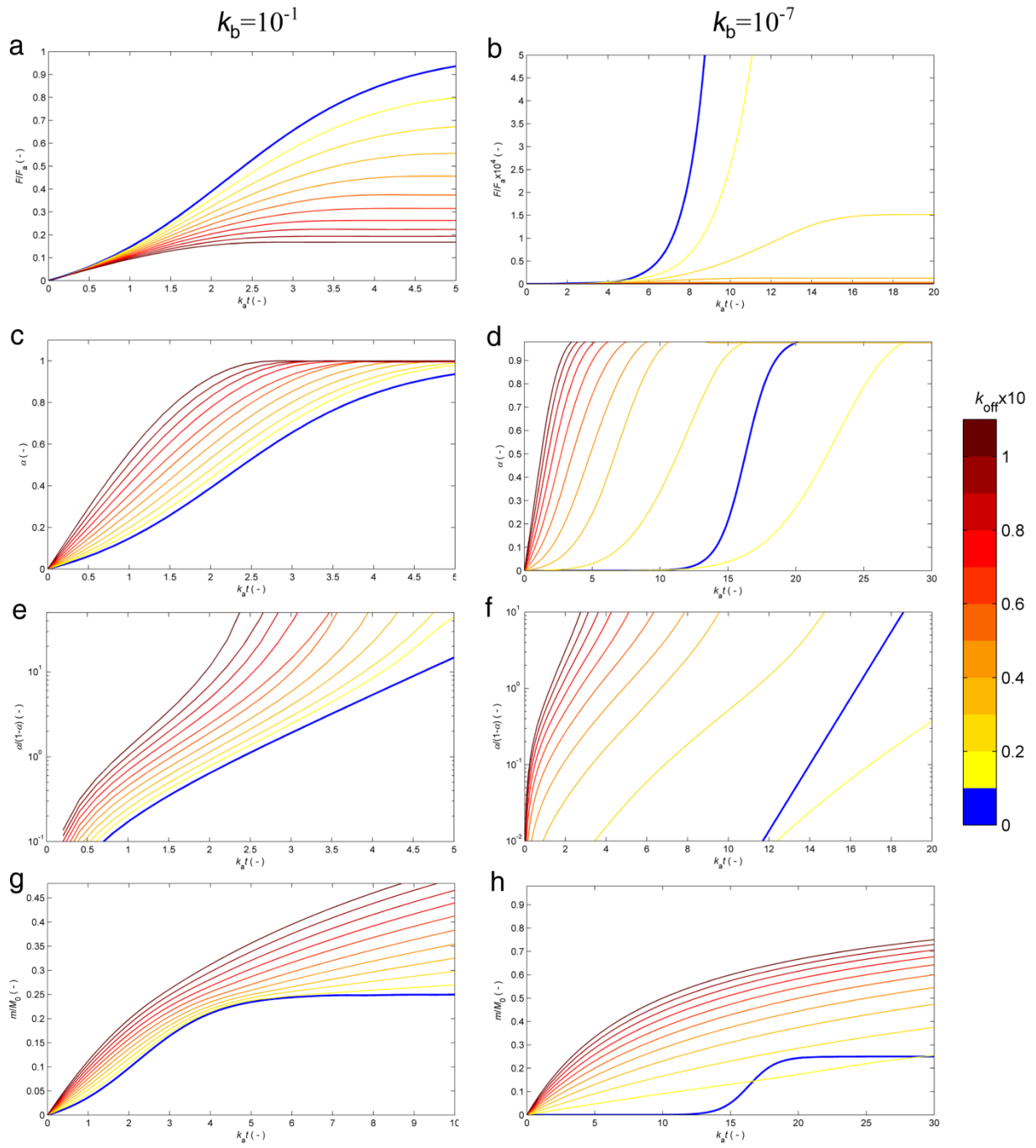


Figure 5

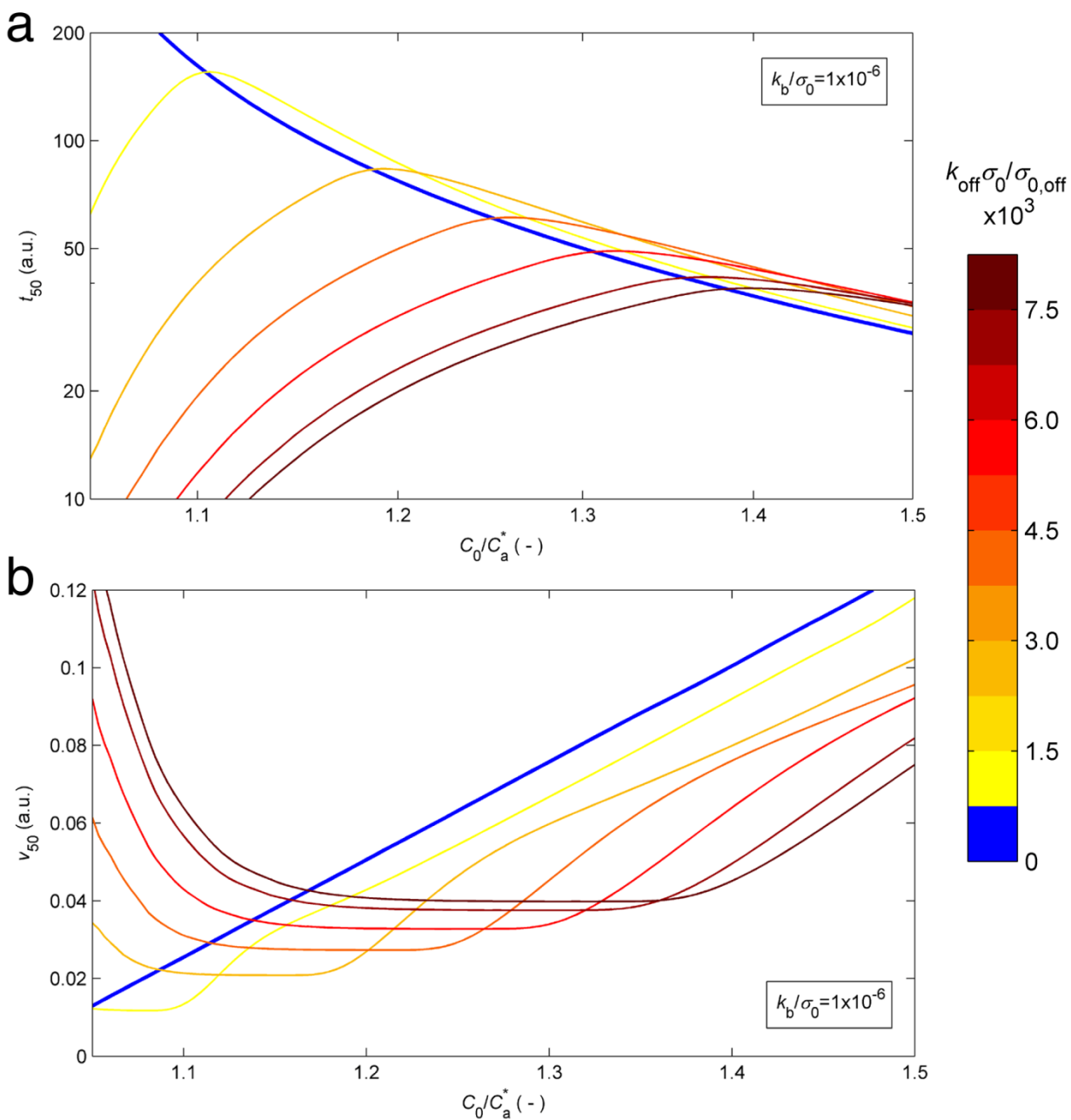


Figure 6

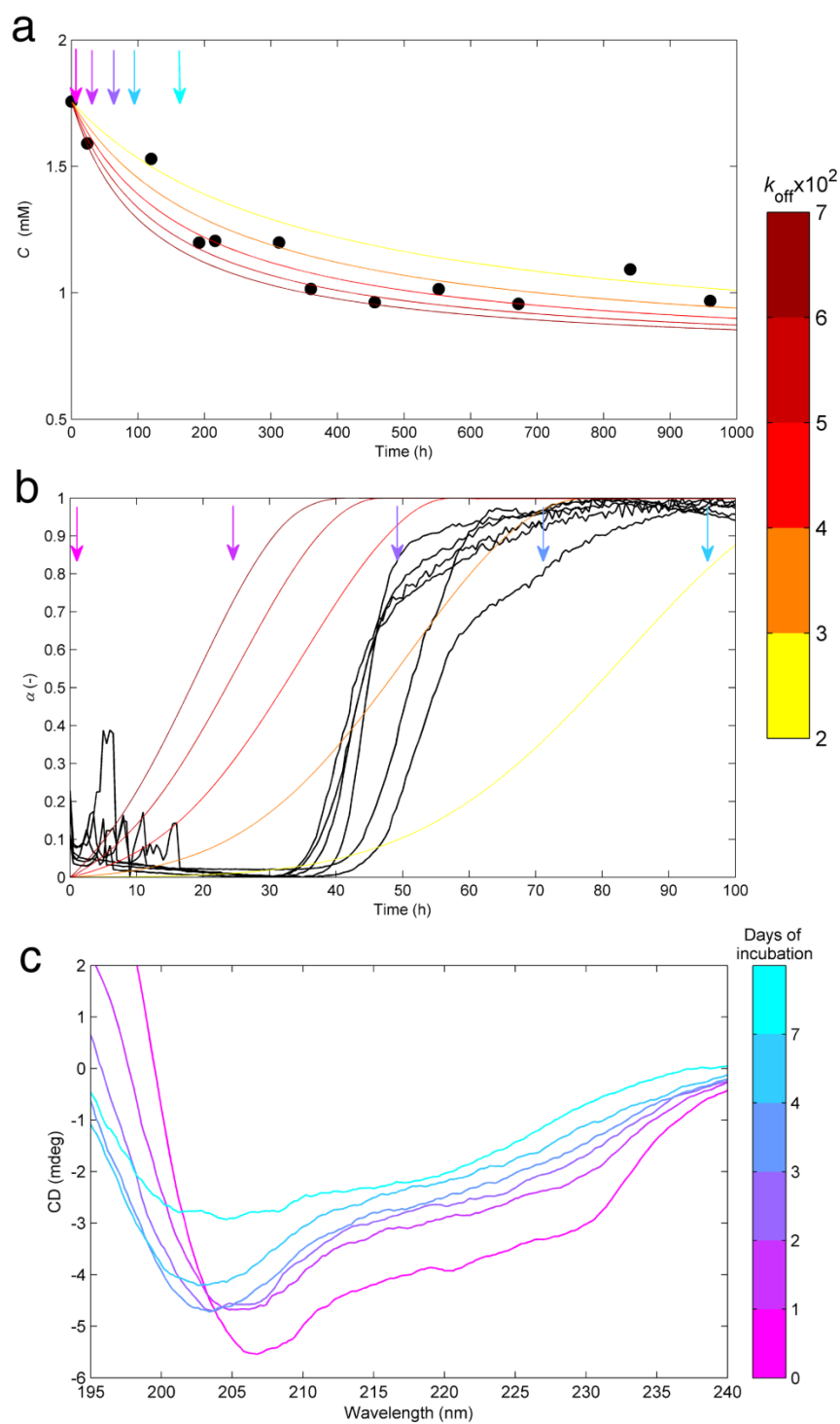


Figure 7

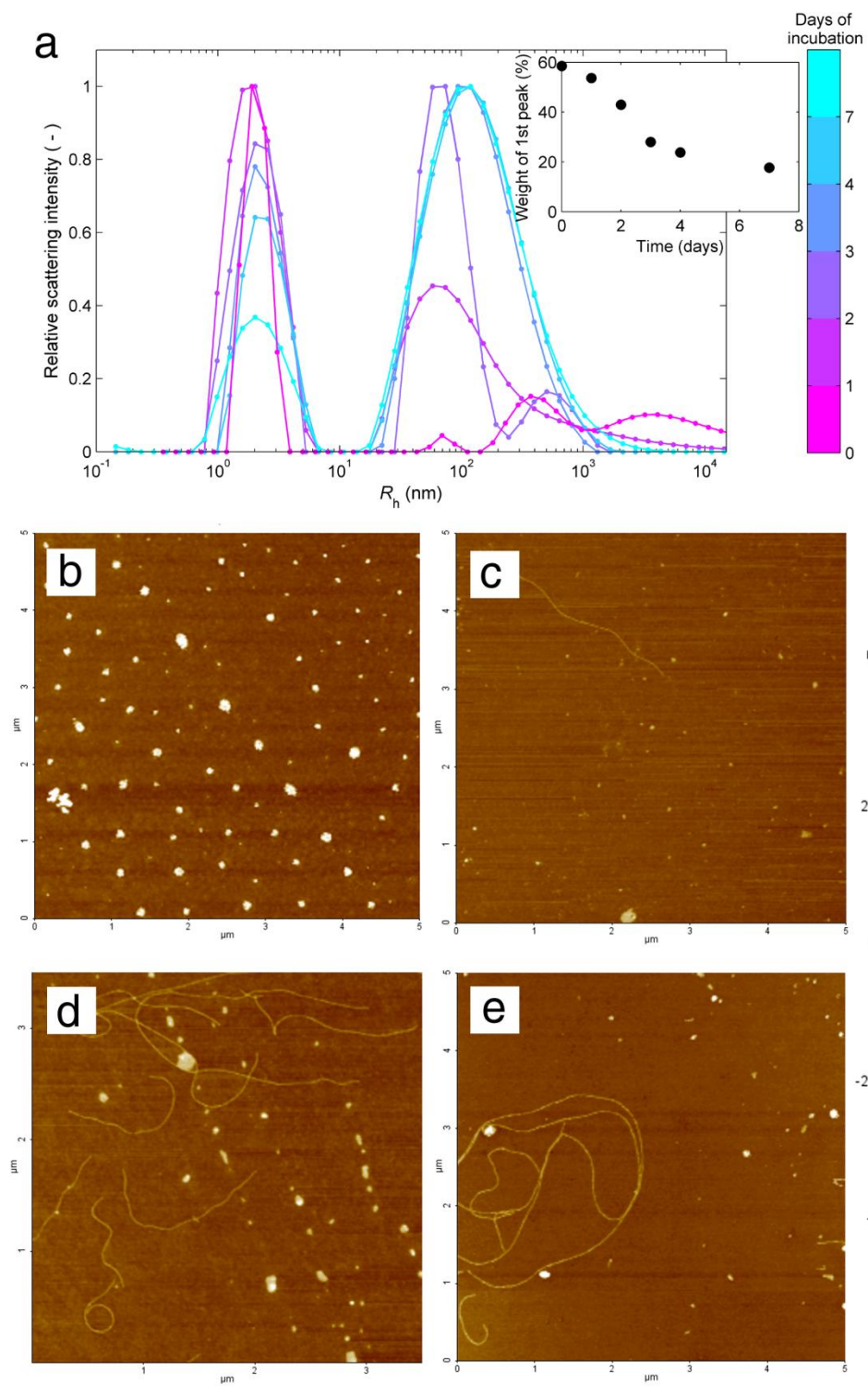
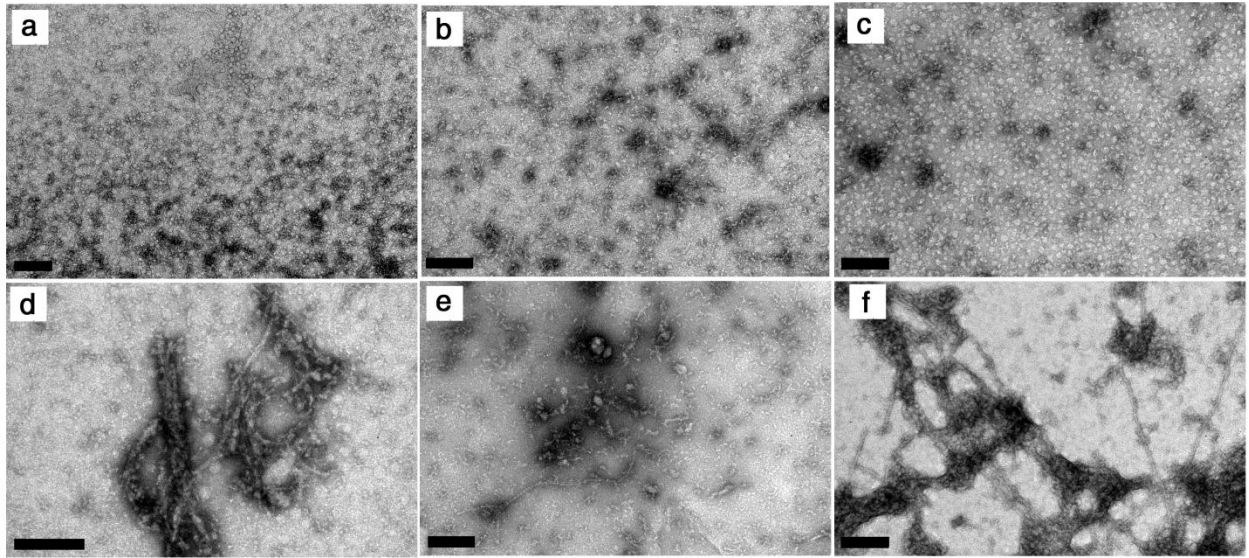


Figure 8



What can the kinetics of amyloid fibril formation tell about off-pathway aggregation?

Rosa Crespo, Eva Villar-Alvarez, Pablo Taboada, Fernando A. Rocha, Ana M. Damas and Pedro M. Martins

J. Biol. Chem. published online November 24, 2015

Access the most updated version of this article at doi: [10.1074/jbc.M115.699348](https://doi.org/10.1074/jbc.M115.699348)

Alerts:

- [When this article is cited](#)
- [When a correction for this article is posted](#)

[Click here](#) to choose from all of JBC's e-mail alerts

This article cites 0 references, 0 of which can be accessed free at <http://www.jbc.org/content/early/2015/11/24/jbc.M115.699348.full.html#ref-list-1>

LEPABE - Laboratory for Process Engineering, Environment, Biotechnology and Energy

